Antarctic Ozone Loss Shapes Surface Cooling Pattern and Climate Sensitivity

Peidong Wang[a,b,#], Susan Solomon[b], Clara Deser[c], David W. J. Thompson[d,e], Noah S. Diffenbaugh[a]

[a]Doerr School of Sustainability, Stanford University, Stanford, CA, USA

[b]Department of Earth, Atmospheric, and Planetary Sciences, Massachusetts Institute of Technology, Cambridge, MA, USA

[c]Climate and Global Dynamics Laboratory, National Center for Atmospheric Research, Boulder, CO, USA

[d]Department of Atmospheric Science, Colorado State University, Fort Collins, CO, USA

[e]School of Environment Sciences, University of East Anglia, Norwich, UK

[#]Correspondence: Peidong Wang (pdwang@stanford.edu)

Changes in sea surface temperature (SST) patterns have recently been recognized as a major feedback affecting the sensitivity of climate to increases in greenhouse gases[1–3]. Over recent decades, while most of Earth's surface warmed, the eastern tropical Pacific and Southern Ocean unexpectedly cooled. These regional SST cooling trends are not reproduced by most global climate models (GCMs)[4], leading to systematic biases in estimates of global climate sensitivity[1,2]. While Antarctic ozone depletion has been proposed as a potential driver of the cooling[5], its influence has previously been considered too weak[6,7]. Here we provide novel evidence that suggests Antarctic ozone depletion can indeed quantitatively account for this observed SST cooling. Using ~4,000 years of simulation from eight GCMs, we construct a multiple linear regression model that isolates the intrinsic relationship between Antarctic ozone and SST, capturing robust short-timescale coupling while avoiding biases from the lack of resolved ocean eddies and their long-timescale adjustments in GCMs[8–10]. We calculate that the ozone-driven SST pattern effect strengthened the global radiative feedback by 17-21% (0.49-0.83 W m^{-2} K^{-1}) during 1979-2000, thereby reducing effective climate sensitivity. As Antarctic ozone starts to recover[11,12], the stabilizing influence has begun to wane, leading to a more warming-prone climate.

Although GCMs capture the historical rise in global-mean surface temperature due to increases in greenhouse gases (GHGs) associated with anthropogenic activities, they fail to reproduce some key spatial features—most notably the cooling trends in the eastern tropical Pacific and the Southern Ocean that have persisted over the past four decades[4]

(Figure 1). This discrepancy between GCMs and observations exemplifies the SST 'pattern effect', in which the spatial pattern of SST influences the strength of climate feedbacks and, in turn, the rate of global warming[13,14]. In particular, cooling in the eastern tropical Pacific promotes low-cloud cover and enhances shortwave reflection, reducing net radiative heating of the climate system[15]. Given the observed SST pattern, recent decades have exhibited stabilizing climate feedbacks, whereas GCMs lack this cooling pattern on average, and therefore imply a system more prone to warming[2]. In addition, the observed eastern tropical Pacific cooling may have influenced climate in remote regions through atmospheric teleconnections, such as drought in the western United States[16]. Therefore, understanding the observed SST cooling pattern is key for interpreting historical climate change, assessing global climate sensitivity, and improving future global and regional climate projections. However, the mechanisms responsible for this cooling signature remain uncertain[17].

Antarctic ozone depletion has been proposed as a potential driver of Southern Ocean SST cooling by strengthening the westerlies at high latitudes and thereby altering wind-driven ocean circulation[5]. This poleward jet shift characterizes a transition to the positive phase of the Southern Annular Mode (SAM) since the 1980s, driven largely by Antarctic ozone depletion[18–20]. Despite this well-established mechanistic link, empirical studies based on linear regression analysis[6] and GCM experiments with prescribed ozone forcing[7] suggest that ozone depletion explains less than 10% of the observed Southern Ocean SST cooling in recent decades. However, both approaches have important limitations. Decadal-scale variability of Southern Ocean SSTs is also influenced

by GHG-driven SAM changes[19,21,22] and is further complicated by remote influences from tropical Pacific SSTs via atmospheric teleconnections[23]. As a result, regressions based on short observational records may confound ozone's effects with other factors. In addition, standard-resolution GCMs (e.g., 1° horizontal resolution) tend to simulate a spurious enhancement of poleward ocean heat transport in response to an increase in the SAM, inconsistent with both observations and results from high-resolution (e.g., 0.1° horizontal resolution), eddy-resolving ocean models[8–10,24]. This warm bias arising from the lack of resolved ocean eddies in the Southern Ocean could substantially dampen the ozone-depletion-induced cooling signal in standard-resolution GCMs, leading to an underestimate of ozone's contribution. Further, recent advances in high-resolution climate models have been carried out with ensemble sizes that are too small to cleanly isolate the forced response from internal variability[25], and running large ensembles with eddy-resolving ocean models that explicitly control ozone forcing remains prohibitively expensive with current computational resources.

SST response to Antarctic ozone depletion

To characterize the simulated intrinsic relationship between Antarctic ozone and SST, we construct a multiple linear regression (MLR) model in which annual-mean SST at each grid point is regressed onto the preceding year's (lag 1-year) September-December polar-cap (60°S-90°S) total column ozone using ~4,000 years of pre-industrial control (PiControl) simulations from eight GCMs archived in Phase 6 of the Coupled Model Intercomparison Project (CMIP6; Extended Data Table 1 and Methods). The selected GCMs employ either simplified or fully interactive stratospheric chemistry[26]. Therefore,

84 despite their fixed pre-industrial levels of ozone-depleting substances, stratospheric
85 ozone exhibits internally generated variability consistent with two-way coupling between
86 ozone and atmospheric dynamics. The advantage of our methodology compared to
87 regressions based on either observations or historical simulations is that the long
88 PiControl simulations eliminate time-varying external forcings and span many phases of
89 low-frequency natural variability, enabling a rich sampling of the simulated ozone-SST
90 relationship. This approach also isolates the surface temperature response to Antarctic
91 ozone changes from the direct radiative forcing due to changes in global ozone and the
92 ozone-depleting substances themselves. The disadvantage is that it relies on the fidelity
93 of the simulated relationships between Antarctic ozone and SST. Acknowledging
94 GCM-specific biases, we ensure robustness by considering only regions where all eight
95 GCMs agree on the sign of the SST response to Antarctic ozone, with the spread of
96 response magnitudes in these areas providing an estimate of inter-model uncertainty.
97 Regression coefficients from individual GCMs and the multi-model-means for each
98 predictor in the MLR are shown in Extended Data Figures 1-3; details of the MLR and
99 additional sensitivity tests are provided in the Methods section.
100
101 To quantify SST responses to historical changes in Antarctic ozone, we apply the multi-
102 model-mean intrinsic ozone-SST relationship derived from PiControl simulations to the
103 satellite-observed Solar Backscatter Ultraviolet (SBUV[27]) ozone dataset. We then
104 compare the inferred SST response against three widely used observation-based SST
105 reconstructions from COBE-SST2 (ref.[28]), ERSSTv6 (refs.[29,30]), and HadISST1 (ref.[31]).
106 The pattern and magnitude of the 1979-2024 SST cooling driven by changes in Antarctic

ozone (Figure 1d) align remarkably well with the three observed SST reconstructions (Figures 1a-c) in the eastern tropical Pacific and Southern Ocean. Averaged over this region, where all eight GCMs exhibit a robust cooling response to declining Antarctic ozone (highlighted by dashed contours in Figures 1a-d), the ozone-explained SST cooling trend based on the MLR model is 0.067 ± 0.027 K dec^{-1} over 1979-2024 (±1σ of the MLR regression coefficients across the eight GCMs), while the three observational SST datasets yield cooling trends of 0.017 (COBE-SST2), 0.065 (ERSSTv6), and 0.042 (HadISST1) K dec^{-1}. The large inter-dataset spread likely reflects the sparse data coverage over the Southern Ocean, which can lead to substantial uncertainties[32]. Nevertheless, the SST cooling trends from all three observational datasets in the eastern tropical Pacific and Southern Ocean fall within the ±2σ uncertainty range of the MLR model explained by observed Antarctic ozone changes.

The observed 22-year running mean Antarctic ozone time series (red curve in Figure 1f) exhibits a pronounced decline from around 1979 to 2000 during the ozone depletion era, followed by a plateau in the recovery period after 2000. Figure 1f also presents the 22-year running-mean SST anomalies from both the observations and predicted by the MLR from the observed ozone time series, averaged over the dashed region in Figures 1a-d. (The unfiltered SST anomalies and the 22-year running mean SST averaged separately over the eastern tropical Pacific and Southern Ocean are shown in Extended Data Figures 4 and 5.) As expected, the regional-mean ozone-explained SSTs from the MLR model (blue curve) mirror the Antarctic ozone time series, showing a rapid cooling from 1979 to 2000 followed by steady conditions thereafter. However, given the large inter-

dataset uncertainties and the influences of interannual and decadal SST variabilities unrelated to Antarctic ozone, it remains challenging to robustly identify a transition from cooling to steady conditions in the observed SST records across the pre- and post-2000 periods.

Previous studies have suggested that Antarctic ozone depletion can produce a broad spatial pattern of cooling that resembles observations, but the simulated response is typically an order of magnitude weaker than observed[6,7]. This raises the question: why can the MLR model, trained on the linkages between Antarctic ozone and SSTs in PiControl simulations, capture the observed magnitude of eastern tropical Pacific and Southern Ocean SST cooling? Studies using standard-resolution GCMs generally find that the Southern Ocean cools in response to an increase in the SAM on short (i.e., annual) timescales but warms on long (i.e., multi-annual and decadal) timescales[8,33,34]. In contrast, recent high-resolution, eddy-resolving ocean models show a consistent short-timescale cooling response but no evidence of significant long-timescale warming response, possibly owing to mesoscale eddy compensation that suppresses the interior upwelling of warm deep water[8]. This distinction is also evident in ocean heat transport, with standard-resolution GCMs exhibiting long-timescale enhanced poleward heat transport in response to an increase in the SAM, opposite to the trends seen in eddy-resolving models and observations[8–10,24]. By regressing SST on the preceding year's Antarctic ozone, our MLR model primarily captures the short-timescale ozone-SST coupling dominated by wind-driven Ekman heat transport, which is well represented in standard-

resolution GCMs, while excluding the spurious long-timescale response associated with the absence of resolved ocean eddies.

The short-timescale coupling between Antarctic ozone and SSTs in the PiControl simulations is evident in lead-lag composites of sea-level pressure (SLP) and 500-hPa geopotential heights (Z500) between low (<10th percentile) and moderate (40th-60th percentile) Antarctic ozone years (Figure 2). Antarctic ozone variability in PiControl simulations arises primarily from El Niño–Southern Oscillation (ENSO): El Niño/La Niña accelerates/slows the Brewer-Dobson circulation in the stratosphere, transporting more/less ozone-rich air poleward[35,36], with ENSO leading Antarctic ozone by ~12 months[37]. Consistent with this mechanism, composite SST anomalies one year before low Antarctic ozone show pronounced La Niña-like cooling in the tropical Pacific (Figure 2a). The accompanying SLP and Z500 anomaly patterns—enhanced west-east tropical Indo-Pacific SLP gradient and broad tropical-mean reduction in Z500 (Figures 2d,g)—likewise reflect the canonical ENSO-troposphere coupling[38,39]. Once La Niña establishes anomalously low Antarctic ozone during austral spring (September-December), ozone exerts its strongest influence on Southern Hemisphere climate in the following summer (January-April). The resulting patterns resemble the positive phase of the SAM, featuring stronger meridional SLP and Z500 gradients associated with a poleward-shifted jet that intensifies equatorward Ekman heat transport, leading to SST cooling in the Southern Ocean[19] (Figures 2b,e,h). Cold air originating over the Southern Ocean is advected equatorward and subsequently amplified and sustained by positive feedbacks in both the

atmosphere and the ocean along the west coast of South America, thereby reinforcing cooling in the southeast and eastern tropical Pacific[40,41].

Impact on historical climate sensitivity

'Pattern effects' associated with the spatial structure of SST trends, including cooling in the eastern tropical Pacific and Southern Ocean, have slowed global warming during the historical period[2,42]. To quantify the contribution of Antarctic ozone depletion and recovery to these pattern effects, we apply a Green's Function approach[1] to estimate the temporal evolution of the global radiative feedback parameter associated with the ozone-induced component of observed SST trends (see Methods). Figure 3 shows the percent contribution from ozone-induced changes in the pattern of SST trends for top-of-atmosphere net radiation (R; negative values indicate outgoing radiation), global-mean surface temperature (T), and the global radiative feedback parameter ($\lambda = R/T$) computed from overlapping 22-year SST trend windows. The corresponding absolute values of these quantities, for the observed SSTs and for SSTs with the ozone-induced component removed, are shown separately in Extended Data Figure 6.

During 1979-2000, when Antarctic ozone depletion was strongest, the resulting ozone-induced SST cooling based on the MLR model was also largest in the eastern tropical Pacific (Extended Data Figure 5a), where radiative feedbacks are particularly sensitive[1,3,15]. We estimate that the ozone-induced SST trend pattern increased the efficiency of radiative cooling to space by 5-7% (0.019-0.022 W m^{-2} dec^{-1}), with the range representing the spread in mean estimates across the three observational SST datasets

(see Methods). At the same time, the ozone-induced SST trend pattern reduced the rate of global surface warming by 15-20% (0.016-0.020 K dec^{-1}). Together, these effects produced a 17-21% (0.49-0.83 W m^{-2} K^{-1}) strengthening of the global radiative feedback parameter (i.e., making λ more negative). In other words, the SST trend pattern induced by ozone depletion enhanced radiative damping by approximately 20%, leading to more energy lost to space per degree of surface warming and a more stable, less warming-prone climate state.

When the analysis is extended into the 21st-century ozone recovery period, the ozone-induced SST cooling in the eastern tropical Pacific becomes weaker and can even reverse sign (Extended Data Figure 5a). As a result, ozone's contribution to enhanced radiative cooling correspondingly diminishes, and global-mean surface warming accelerates. This shift yields a less stable, more warming-prone climate state, reflected in a positive change in λ of 3-4% or 0.06-0.12 W m^{-2} K^{-1} during 1999-2020. Notably, the time-varying climate sensitivity we diagnose, arising from ozone-induced SST pattern changes, closely matches the behavior reported in ref.[2], which identified a substantially lower-sensitivity climate state emerging after the 1980s relative to that expected from long-term CO_2 increases, followed by a gradual waning of this difference after the 2000s.

SST pattern effect under ozone recovery

Due to declines in ozone-depleting substances, signs of Antarctic ozone recovery have already emerged in the 21st century[11,12]. However, because of the large natural variability in ozone and the short observational record, along with the exceptional 2020 Australian

wildfires and the 2022 Hunga-Tonga volcanic eruption that contributed to additional ozone losses[43,44], the SSTs explained by observed ozone still show a weak cooling trend in the eastern tropical Pacific and Southern Ocean during 2000-2024 (Figure 4a). In contrast, simulated multi-model-mean ozone, which combines historical and SSP2-4.5 forcings, exhibits much reduced natural variability and does not include the recent exceptional wildfire- and volcano-driven ozone losses (see Methods). As a result, the SSTs explained by modeled ozone reverse sign and show a warming pattern in response to the modeled increase in Antarctic ozone during 2000-2024 (Figures 4b-c).

Under the SSP2-4.5 scenario, Antarctic ozone is projected to return to 1980 levels by the middle of the 21st century[26], implying that the SST cooling in the eastern tropical Pacific and Southern Ocean induced by ozone depletion, and the associated shift toward a more negative global radiative feedback since ~1980, should likewise subside by the 2050s (Figure 4c). Note that the SST projections in Figure 4c reflect only the response to changes in Antarctic ozone. As ozone recovery proceeds more gradually than the preceding rapid depletion, future changes in other factors such as anthropogenic aerosols[45,46], GHGs[47], and Antarctic ice-sheet melt[48] may increasingly dominate SST evolution and influence the timing of the 'de-emergence' of the SST pattern effect associated with Antarctic ozone recovery.

Summary and conclusions

In summary, we provide numerical evidence that observed SST cooling in the eastern tropical Pacific and Southern Ocean can be quantitatively explained by Antarctic ozone

depletion. This evidence is based on a MLR model developed from the statistics of interannual ozone-SST dynamical coupling in unforced (PiControl) simulations, which avoids biases arising from unresolved ocean eddy adjustments on longer timescales in standard-resolution GCMs. This ozone-depletion-induced SST trend pattern has contributed to a decrease in global climate sensitivity in recent decades, strengthening the global radiative feedback by ~20% during 1979-2000. Likewise, if Antarctic ozone continues to recover from its minimum around the turn of the 21st century, the global radiative feedback is expected to shift toward a higher-sensitivity, more warming-prone climate. In this context, it is important to emphasize that the climate sensitivity results presented here isolate only the ozone-induced SST pattern effect and do not represent the full range of radiative, chemical, and dynamical benefits associated with ozone recovery, which remain essential for climate and environmental protection. More broadly, these findings highlight Antarctic ozone as a key regulator of global climate through its previously underestimated impact on SST pattern effects, and underscore the importance of representing chemistry-climate interactions in the coupled stratosphere-troposphere-ocean system for improved understanding of historical and future climate change.

References

1. Dong, Y., Proistosescu, C., Armour, K. C. & Battisti, D. S. Attributing Historical and Future Evolution of Radiative Feedbacks to Regional Warming Patterns using a Green's Function Approach: The Preeminence of the Western Pacific. *Journal of Climate* **32**, 5471–5491 (2019).

2. Andrews, T. *et al.* On the Effect of Historical SST Patterns on Radiative Feedback. *Journal of Geophysical Research: Atmospheres* **127**, e2022JD036675 (2022).
3. Alessi, M. J. & Rugenstein, M. A. A. Surface Temperature Pattern Scenarios Suggest Higher Warming Rates Than Current Projections. *Geophysical Research Letters* **50**, e2023GL105795 (2023).
4. Wills, R. C. J., Dong, Y., Proistosecu, C., Armour, K. C. & Battisti, D. S. Systematic Climate Model Biases in the Large-Scale Patterns of Recent Sea-Surface Temperature and Sea-Level Pressure Change. *Geophysical Research Letters* **49**, e2022GL100011 (2022).
5. Hartmann, D. L. The Antarctic ozone hole and the pattern effect on climate sensitivity. *Proceedings of the National Academy of Sciences* **119**, e2207889119 (2022).
6. Dong, Y., Polvani, L. M. & Bonan, D. B. Recent Multi-Decadal Southern Ocean Surface Cooling Unlikely Caused by Southern Annular Mode Trends. *Geophysical Research Letters* **50**, e2023GL106142 (2023).
7. Dong, Y., Polvani, L. M., Hwang, Y.-T. & England, M. R. Stratospheric ozone depletion has contributed to the recent tropical La Niña-like cooling pattern. *npj Climate and Atmospheric Science* **8**, 150 (2025).
8. Doddridge, E. W. *et al.* Eddy Compensation Dampens Southern Ocean Sea Surface Temperature Response to Westerly Wind Trends. *Geophysical Research Letters* **46**, 4365–4377 (2019).
9. Bilgen, S. I. & Kirtman, B. P. Impact of ocean model resolution on understanding the delayed warming of the Southern Ocean. *Environmental Research Letters* **15**, 114012 (2020).

10. Yeager, S. G. *et al.* Reduced Southern Ocean warming enhances global skill and signal-to-noise in an eddy-resolving decadal prediction system. *npj Climate and Atmospheric Science* **6**, 107 (2023).
11. Solomon, S. *et al.* Emergence of healing in the Antarctic ozone layer. *Science* **353**, 269–274 (2016).
12. Wang, P. *et al.* Fingerprinting the recovery of Antarctic ozone. *Nature* **639**, 646–651 (2025).
13. Stevens, B., Sherwood, S. C., Bony, S. & Webb, M. J. Prospects for narrowing bounds on Earth's equilibrium climate sensitivity. *Earth's Future* **4**, 512–522 (2016).
14. Armour, K. C., Bitz, C. M. & Roe, G. H. Time-Varying Climate Sensitivity from Regional Feedbacks. *Journal of Climate* **26**, 4518–4534 (2013).
15. Zhou, C., Zelinka, M. D. & Klein, S. A. Analyzing the dependence of global cloud feedback on the spatial pattern of sea surface temperature change with a Green's function approach. *Journal of Advances in Modeling Earth Systems* **9**, 2174–2189 (2017).
16. Seager, R. *et al.* Causes of the 2011–14 California Drought. *Journal of Climate* **28**, 6997–7024 (2015).
17. Watanabe, M. *et al.* Possible shift in controls of the tropical Pacific surface warming pattern. *Nature* **630**, 315–324 (2024).
18. Thompson, D. W. J. & Solomon, S. Interpretation of Recent Southern Hemisphere Climate Change. *Science* **296**, 895–899 (2002).
19. Thompson, D. W. J. *et al.* Signatures of the Antarctic ozone hole in Southern Hemisphere surface climate change. *Nature Geoscience* **4**, 741–749 (2011).

20. Polvani, L. M., Waugh, D. W., Correa, G. J. P. & Son, S.-W. Stratospheric Ozone Depletion: The Main Driver of Twentieth-Century Atmospheric Circulation Changes in the Southern Hemisphere. *Journal of Climate* **24**, 795–812 (2011).
21. Arblaster, J. M. & Meehl, G. A. Contributions of External Forcings to Southern Annular Mode Trends. *Journal of Climate* **19**, 2896–2905 (2006).
22. Kostov, Y., Ferreira, D., Armour, K. C. & Marshall, J. Contributions of Greenhouse Gas Forcing and the Southern Annular Mode to Historical Southern Ocean Surface Temperature Trends. *Geophysical Research Letters* **45**, 1086–1097 (2018).
23. Watanabe, M., Dufresne, J.-L., Kosaka, Y., Mauritsen, T. & Tatebe, H. Enhanced warming constrained by past trends in equatorial Pacific sea surface temperature gradient. *Nature Climate Change* **11**, 33–37 (2021).
24. Armour, K. C., Marshall, J., Scott, J. R., Donohoe, A. & Newsom, E. R. Southern Ocean warming delayed by circumpolar upwelling and equatorward transport. *Nature Geoscience* **9**, 549–554 (2016).
25. Dhame, S., Olonscheck, D. & Rugenstein, M. Higher-Resolution Climate Models Do Not Consistently Reproduce the Observed Tropical Pacific Warming Pattern. *Journal of Climate* **38**, 3131–3149 (2025).
26. Keeble, J. *et al.* Evaluating stratospheric ozone and water vapour changes in CMIP6 models from 1850 to 2100. *Atmospheric Chemistry and Physics* **21**, 5015–5061 (2021).
27. McPeters, R. D., Bhartia, P. K., Haffner, D., Labow, G. J. & Flynn, L. The version 8.6 SBUV ozone data record: An overview. *Journal of Geophysical Research: Atmospheres* **118**, 8032–8039 (2013).

28. Hirahara, S., Ishii, M. & Fukuda, Y. Centennial-Scale Sea Surface Temperature Analysis and Its Uncertainty. *Journal of Climate* **27**, 57–75 (2014).
29. Huang, B. *et al.* Extended Reconstructed Sea Surface Temperature, Version 6 (ERSSTv6). Part I: An Artificial Neural Network Approach. *Journal of Climate* **38**, 1105–1121 (2025).
30. Huang, B. *et al.* Extended Reconstructed Sea Surface Temperature, Version 6 (ERSSTv6). Part II: Upgrades on Quality Control and Large-Scale Filter. *Journal of Climate* **38**, 1123–1136 (2025).
31. Rayner, N. A. *et al.* Global analyses of sea surface temperature, sea ice, and night marine air temperature since the late nineteenth century. *Journal of Geophysical Research: Atmospheres* **108**, (2003).
32. Cooper, V. T., Hakim, G. J. & Armour, K. C. Monthly Sea Surface Temperature, Sea Ice, and Sea Level Pressure over 1850–2023 from Coupled Data Assimilation. *Journal of Climate* **38**, 5461–5490 (2025).
33. Ferreira, D., Marshall, J., Bitz, C. M., Solomon, S. & Plumb, A. Antarctic Ocean and Sea Ice Response to Ozone Depletion: A Two-Time-Scale Problem. *Journal of Climate* **28**, 1206–1226 (2015).
34. Kostov, Y. *et al.* Fast and slow responses of Southern Ocean sea surface temperature to SAM in coupled climate models. *Climate Dynamics* **48**, 1595–1609 (2017).
35. Calvo, N., Garcia, R. R., Randel, W. J. & Marsh, D. R. Dynamical Mechanism for the Increase in Tropical Upwelling in the Lowermost Tropical Stratosphere during Warm ENSO Events. *Journal of the Atmospheric Sciences* **67**, 2331–2340 (2010).

36. Abalos, M., Legras, B., Ploeger, F. & Randel, W. J. Evaluating the advective Brewer-Dobson circulation in three reanalyses for the period 1979–2012. *Journal of Geophysical Research: Atmospheres* **120**, 7534–7554 (2015).
37. He, H. *et al.* Lagged ENSO teleconnection mechanisms driving Antarctic stratospheric ozone depletion variability. *Atmospheric Research* **329**, 108539 (2026).
38. Bjerknes, J. Atmospheric Teleconnections from the Equatorial Pacific. *Monthly Weather Review* **97**, 163–172 (1969).
39. Trenberth, K. E. & Smith, L. The Vertical Structure of Temperature in the Tropics: Different Flavors of El Niño. *Journal of Climate* **19**, 4956–4973 (2006).
40. Kim, H., Kang, S. M., Kay, J. E. & Xie, S.-P. Subtropical clouds key to Southern Ocean teleconnections to the tropical Pacific. *Proceedings of the National Academy of Sciences* **119**, e2200514119 (2022).
41. Kang, S. M. *et al.* Global impacts of recent Southern Ocean cooling. *Proceedings of the National Academy of Sciences* **120**, e2300881120 (2023).
42. Armour, K. C. *et al.* Sea-surface temperature pattern effects have slowed global warming and biased warming-based constraints on climate sensitivity. *Proceedings of the National Academy of Sciences* **121**, e2312093121 (2024).
43. Solomon, S. *et al.* Chlorine activation and enhanced ozone depletion induced by wildfire aerosol. *Nature* **615**, 259–264 (2023).
44. Wang, X. *et al.* Stratospheric Climate Anomalies and Ozone Loss Caused by the Hunga Tonga-Hunga Ha'apai Volcanic Eruption. *Journal of Geophysical Research: Atmospheres* **128**, e2023JD039480 (2023).

45. Smith, D. M. *et al.* Role of volcanic and anthropogenic aerosols in the recent global surface warming slowdown. *Nature Climate Change* **6**, 936–940 (2016).
46. Hwang, Y.-T., Xie, S.-P., Chen, P.-J., Tseng, H.-Y. & Deser, C. Contribution of anthropogenic aerosols to persistent La Niña-like conditions in the early 21st century. *Proceedings of the National Academy of Sciences* **121**, e2315124121 (2024).
47. Seager, R. *et al.* Strengthening tropical Pacific zonal sea surface temperature gradient consistent with rising greenhouse gases. *Nature Climate Change* **9**, 517–522 (2019).
48. Schloesser, F., Friedrich, T., Timmermann, A., DeConto, R. M. & Pollard, D. Antarctic iceberg impacts on future Southern Hemisphere climate. *Nature Climate Change* **9**, 672–677 (2019).

Methods

Observation and model descriptions

We consider three widely used, global, gridded SST datasets from 1979 to 2024: the Japan Meteorological Agency Centennial Observation-Based Estimates of SSTs (COBE-SST2; ref.[28]), the U.S. National Oceanic and Atmospheric Administration Extended Reconstructed SST (ERSSTv6; refs.[29,30]), and the U.K. Met Office Hadley Centre Sea Ice and Sea Surface Temperature dataset (HadISST1; ref.[31]). These datasets are reconstructed primarily from *in situ* ship and buoy measurements, with HadISST1 further supplemented by satellite observations after the 1980s. The Southern Ocean remains the region with the sparsest observational coverage, even after 1980 (ref.[32]), resulting in substantial inter-dataset uncertainties. To account for this observational uncertainty, we include all three reconstructed SST products in our analysis.

We consider satellite observations of total column ozone from the Solar Backscatter Ultraviolet (SBUV) version 8.7 (ref.[27]), which provides a monthly and zonally averaged ozone dataset from 1970 to 2023. We use the period from 1978 to 2023 to predict ozone-explained SSTs for the period from 1979 to 2024. The SBUV observations have been validated against ground-based Dobson and Brewer measurements and are widely used in past ozone assessments to characterize long-term global and polar ozone changes[49,50].

The models used to construct the MLR in this study are based on PiControl simulations from eight CMIP6 GCMs that employ either simplified or fully interactive stratospheric chemistry schemes. For consistency, we use 499 years from each GCM, although some (e.g., MRI-ESM2-0 and UKESM1-0-LL) provide longer PiControl simulations. To remove any potential model drifts in the PiControl simulations, all variables are linearly detrended on a monthly basis at each grid point. We also use one realization from each GCM's historical simulation (up to 2014) and the SSP2-4.5 scenario (after 2014) in certain analyses (Figures 1e and 4b,c). Since two of the eight GCMs do not provide SSP simulations, the multi-model-mean after 2014 is calculated from the remaining six models. The list of GCMs used is summarized in Extended Data Table 1, and additional details, including their respective chemistry schemes, are provided in ref.[26].

Multiple linear regression and sensitivity tests

We construct the following MLR for each CMIP6 GCM using its 499 years of PiControl simulations to characterize the intrinsic relationship between Antarctic ozone and SST:

$$SST(i,j,t) = \alpha(i,j) \cdot Ozone(t-1) + \beta_1(i,j) \cdot ENSO(t-1) + \beta_2(i,j) \cdot ENSO(t) + \epsilon \qquad (1)$$

where the annual-mean SST anomaly at each grid point (*i*,*j*) in year *t* is regressed onto September-December total column ozone anomaly averaged over 60°S-90°S from the preceding year (*t*-1), and the ENSO indices, calculated as annual-mean SST anomalies averaged over the Niño 3.4 region (5°N-5°S, 170°W-120°W) in years *t*-1 and *t*. ENSO indices are included as additional predictors because Antarctic ozone variability is partly modulated by ENSO teleconnections[51], which also influence global SST directly, with ENSO leading SST by about 0-1.5 years[52]. Including both lag 1-year and lag 0-year ENSO indices allows the partial regression coefficient on Antarctic ozone to capture, as far as possible, the local ozone influence on SST.

Given differences in model physics, some GCMs (e.g., CNRM-CM6-1 and E3SM-1-0) exhibit a stronger SST response to Antarctic ozone, whereas others (e.g., GFDL-ESM4) show a weaker response, as illustrated by the partial regression coefficients for Antarctic ozone in individual GCMs (Extended Data Figures 1a-h). Our analysis focuses on regions where all eight GCMs agree on the sign of the SST response to Antarctic ozone, highlighted by dashed contours in the multi-model-mean (Extended Data Figure 1i). We also include ±1σ of the multi-model-mean coefficients to represent uncertainty associated with GCM differences. Applying this criterion, the eastern tropical Pacific and the Southern Ocean both emerge as regions with a robust SST response to Antarctic ozone variability. In both regions, all GCMs yield positive coefficients, indicating SST cooling with Antarctic ozone depletion (i.e., lower ozone). The warming in the South Indian Ocean (in response to a decrease in Antarctic ozone) and the dipole pattern in the South Atlantic Ocean are also consistent with SAM-based regression from observations[5]. Importantly, this robust

447 inter-model agreement between Antarctic ozone and SST is largely confined to the
448 Southern Hemisphere, suggesting that ENSO teleconnections are effectively minimized
449 in the partial regression on Antarctic ozone.
450
451 We conduct additional sensitivity tests to examine the robustness and physical linkage
452 between Antarctic ozone and SST. The key relationship between Antarctic ozone loss
453 during springtime and lower-than-normal SSTs in the eastern tropical Pacific and the
454 Southern Ocean is both robust across different analysis designs and consistent with
455 physical expectations. For instance, similar patterns and magnitudes emerge in MLR
456 analyses using Antarctic ozone averaged in September-October (Extended Data Figure
457 7b) and November-December (Extended Data Figure 7c). In contrast, this relationship
458 disappears when using Antarctic ozone averaged in March-April (Extended Data Figure
459 7d), when no physical connection is expected between Antarctic ozone and SST.
460
461 We further test a simple linear regression between Antarctic ozone and SST. The Pearson
462 correlation coefficients r from the multi-model-mean based on eight CMIP6 PiControl
463 simulations are shown in Extended Data Figure 8a, and the corresponding SST trends
464 derived from this simple linear regression are shown in Extended Data Figure 8b. Non-
465 trivial SST trends appear in the deep tropics and in the Northern Hemisphere, suggesting
466 that ENSO teleconnections may not be fully removed in such a simple linear regression.
467 Nevertheless, the dashed regions, where all eight GCMs show a consistent SST
468 response to Antarctic ozone, are still confined to the Southern Hemisphere and closely
469 align with those identified from the MLR analysis. Moreover, the magnitude of the cooling

over the eastern tropical Pacific and the Southern Ocean remains comparable to that obtained from the MLR (Extended Data Figure 8b and Figure 1d), underscoring the robustness of the ozone-SST relationship in these regions.

Greens function approach for climate sensitivity analysis

The Green's function approach enables us to quantify how a given SST pattern modulates the global climate feedback[1,3,15,53], defined as the global radiative response per degree of global-mean surface temperature change:

$$\lambda = \frac{R}{T} = \frac{\sum_{i,j} GF_R(i,j) \cdot SST_{trend}(i,j)}{\sum_{i,j} GF_T(i,j) \cdot SST_{trend}(i,j)} \quad (2)$$

where *R* and *T* represent the trends in top-of-atmosphere net radiation (units in W m^{-2} dec^{-1}) and global-mean surface temperature (units in K dec^{-1}), obtained by integrating the Green's functions for radiation (GF_R) and surface temperature (GF_T) with a given SST trend pattern (SST_{trend}) globally. The resulting λ (units in W m^{-2} K^{-1}) represents the global radiative feedback associated with the SST trend pattern over the given trend period.

The Green's functions used in this study are taken from ref.[1], derived from the CESM-CAM4 with a horizontal resolution of approximately 1.9° × 2.5°. To ensure consistent spatial integration, all datasets (including observations and CMIP6 outputs) are first re-gridded to this same horizontal resolution. We note that the Green's function applied here is based on a single GCM; however, recent multi-model intercomparison efforts have produced additional Green's functions that capture a wider range of model physics[53], and the Green's function from ref.[1] remains broadly consistent with those derived from other GCMs.

We apply a sliding 22-year trend window from 1979 to 2024 to capture the gradual transition from the ozone-depletion era (mainly 1979-2000) to the ozone-recovery era (after 2000). We calculate R, T, and λ for the observed SST trend patterns using three observation-based SST datasets, representing real-world trends that include both external forcings and internal variability. For each observed SST dataset, we also subtract the ozone-explained SST component to estimate R, T, and λ representing a hypothetical world without ozone-induced SST changes. The subtraction is applied only over regions where all eight GCMs agree on the sign of the SST response to Antarctic ozone (dashed regions in Extended Data Figure 1i), including robust SST cooling in the eastern tropical Pacific and the Southern Ocean and warming in the South Indian Ocean and South Atlantic Ocean due to Antarctic ozone depletion. The resulting R, T, and λ for each SST dataset, based on SSTs with and without ozone-induced changes (represented as solid and dashed curves, respectively), are shown in Extended Data Figure 6. Because observed SST trends are subject to large uncertainties and are therefore sensitive to the choice of endpoints across datasets (e.g., Extended Data Figure 6), we focus on the relative difference between the observed and ozone-removed SST trend patterns within each dataset (Figure 3), for which all three SST products provide consistent results.

Additional references for the Methods section

49. Hassler, B. & Young, P. J. *Scientific Assessment of Ozone Depletion: 2022. Chapter 3: Update on Global Ozone: Past, Present, and Future*. 509 (2022).

50. Chipperfield, M. P. & Santee, M. L. *Scientific Assessment of Ozone Depletion: 2022. Chapter 4: Polar Stratospheric Ozone: Past, Present & Future*. 509 (2022).
51. Domeisen, D. I. V., Garfinkel, C. I. & Butler, A. H. The Teleconnection of El Niño Southern Oscillation to the Stratosphere. *Reviews of Geophysics* **57**, 5–47 (2019).
52. Lin, J. & Qian, T. A New Picture of the Global Impacts of El Nino-Southern Oscillation. *Scientific Reports* **9**, 17543 (2019).
53. Bloch-Johnson, J. *et al.* The Green's Function Model Intercomparison Project (GFMIP) Protocol. *Journal of Advances in Modeling Earth Systems* **16**, e2023MS003700 (2024).

Acknowledgments

P.W. gratefully acknowledges helpful discussions with Yue Dong. P.W. acknowledges support by the Stanford Science Fellowship. P.W. and S.S. acknowledge support from NSF-AGS grant 2316980. N.S.D. acknowledges support from Stanford University. Parts of the computing for this project was performed on high-performance computing resources supported by the Stanford Research Computing Center and the Stanford Doerr School of Sustainability Center for Computation. We acknowledge the World Climate Research Programme, which, through its Working Group on Coupled Modelling, coordinated and promoted CMIP6. We thank the climate modeling groups for producing and making available their model output, the Earth System Grid Federation (ESGF) for archiving the data and providing access, and the multiple funding agencies who support CMIP6 and ESGF.

Data Availability

CMIP6 data are archived at the Earth System Grid Federation (https://aims2.llnl.gov/). COBE-SST2 data are available from the NOAA Physical Sciences Laboratory (https://psl.noaa.gov/data/gridded/data.cobe2.html), ERSSTv6 from the NOAA National Centers for Environmental Information (https://www.ncei.noaa.gov/products/extended-reconstructed-sst), and HadISST1 from the U.K. Met Office (https://www.metoffice.gov.uk/hadobs/hadisst/). The SBUV ozone dataset is available from the NASA Goddard Space Flight Center (https://acd-ext.gsfc.nasa.gov/Data_services/merged/). All CMIP6 and observational SST datasets were re-gridded to a common horizontal resolution, and the re-gridded datasets are available at Zenodo (https://doi.org/10.5281/zenodo.18169353).

Code Availability

The code used to generate all of the figures in this analysis is available at Zenodo (https://doi.org/10.5281/zenodo.18169353).

Author Contributions

P.W. designed the study, analyzed the data, and drafted the initial manuscript. S.S., C.D., D.W.J.T., and N.S.D. contributed significantly to the interpretation of findings and revised the manuscript.

Competing Interests

The authors declare no competing interests.

560

561 **Correspondence and requests for materials**

562 Peidong Wang (pdwang@stanford.edu)

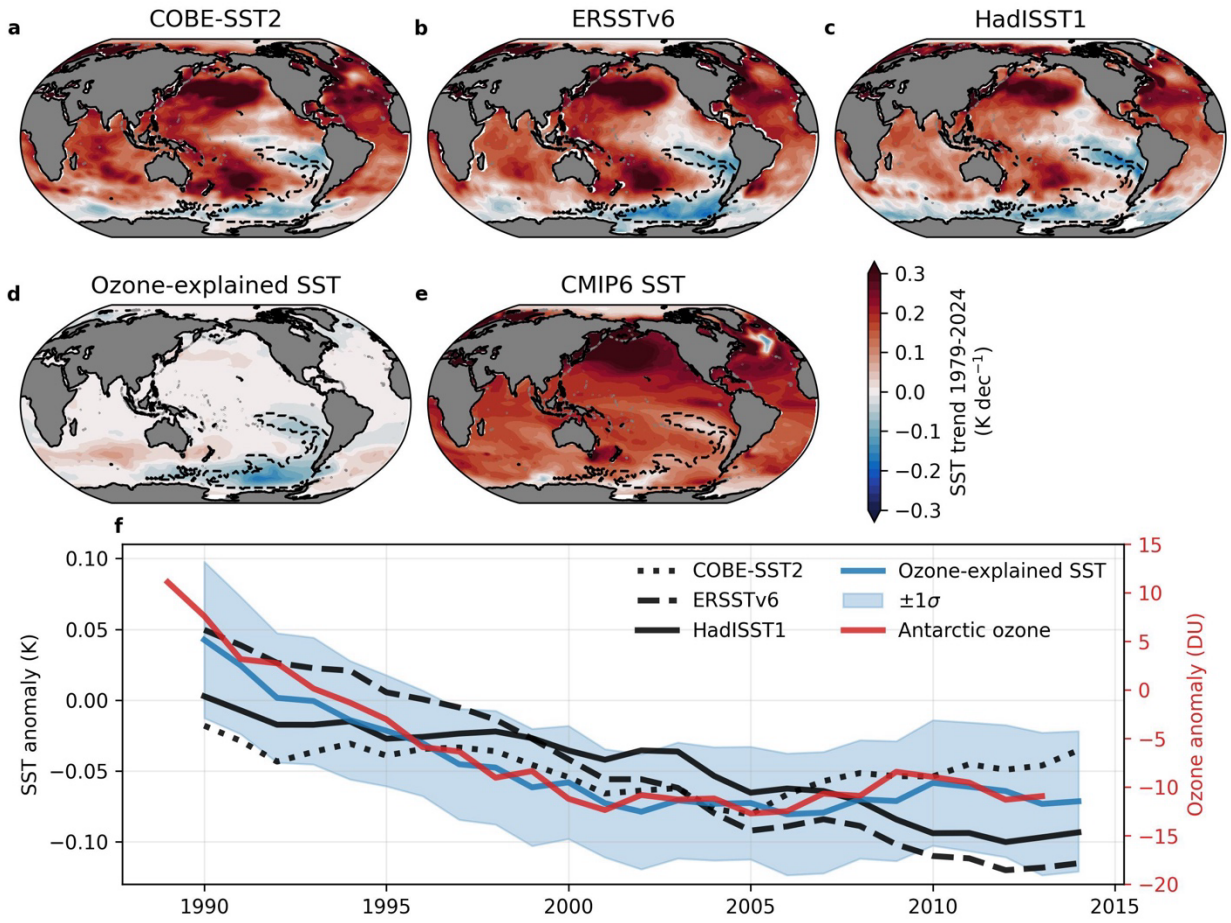

Figure 1. Comparison of observed and modeled sea surface temperature trends. Panels a-e show linear SST trend maps from 1979 to 2024. Panels a-c show observations from three SST datasets (COBE-SST2, ERSSTv6, and HadISST1, respectively). Panel d shows the multi-model-mean ozone-explained SST from the MLR based on eight GCMs (Extended Data Table 1). Panel e shows the multi-model-mean direct SST output from the same eight GCMs. Panel f shows 22-year running-mean SST anomalies averaged over the eastern tropical Pacific and Southern Ocean (region enclosed by the dashed contours in a-e where all eight GCMs agree in the sign of the ozone-induced SST response). Black (solid, dashed, and dotted) curves denote three different SST observations, the blue curve shows the MLR-predicted SST with ±1σ shading indicating uncertainties from regression coefficients, and the red curve (right y-axis) shows the 22-year running-mean September-December total column ozone anomaly averaged over 60°S-90°S.

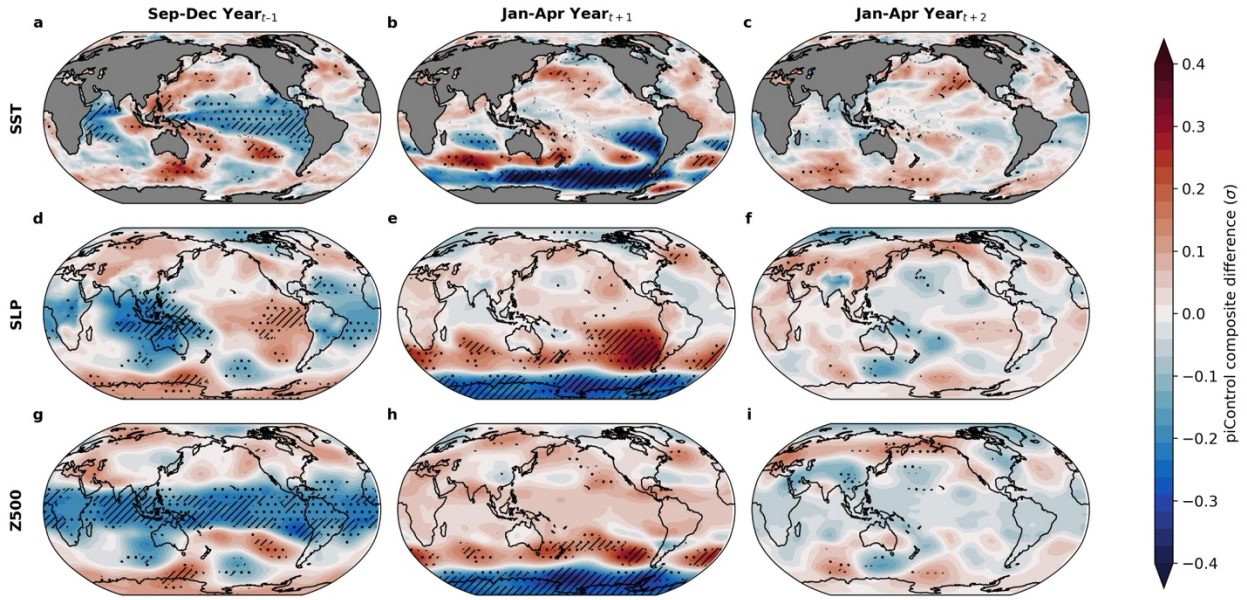

577

578 **Figure 2. Composite sea surface temperature and atmospheric circulation**
579 **anomalies associated with low Antarctic ozone.** Panels a-i show multi-model-mean
580 composite differences between low Antarctic ozone years (<10th percentile) and moderate
581 Antarctic ozone years (40th-60th percentile) in the eight CMIP6 PiControl simulations.
582 Differences in SST (a,b,c), SLP (d,e,f), and Z500 (g,h,i) are shown for the austral spring
583 one year prior to low Antarctic ozone (a,d,g), the subsequent austral summer (b,e,h), and
584 the austral summer two years later (c,f,i). Each field is normalized by its own standard
585 deviation within each GCM's PiControl run before averaging across the eight GCMs,
586 resulting in anomalies in units of σ. Hatching indicates regions where all eight GCMs
587 agree on sign, and dots mark regions where seven of eight GCMs agree on sign.

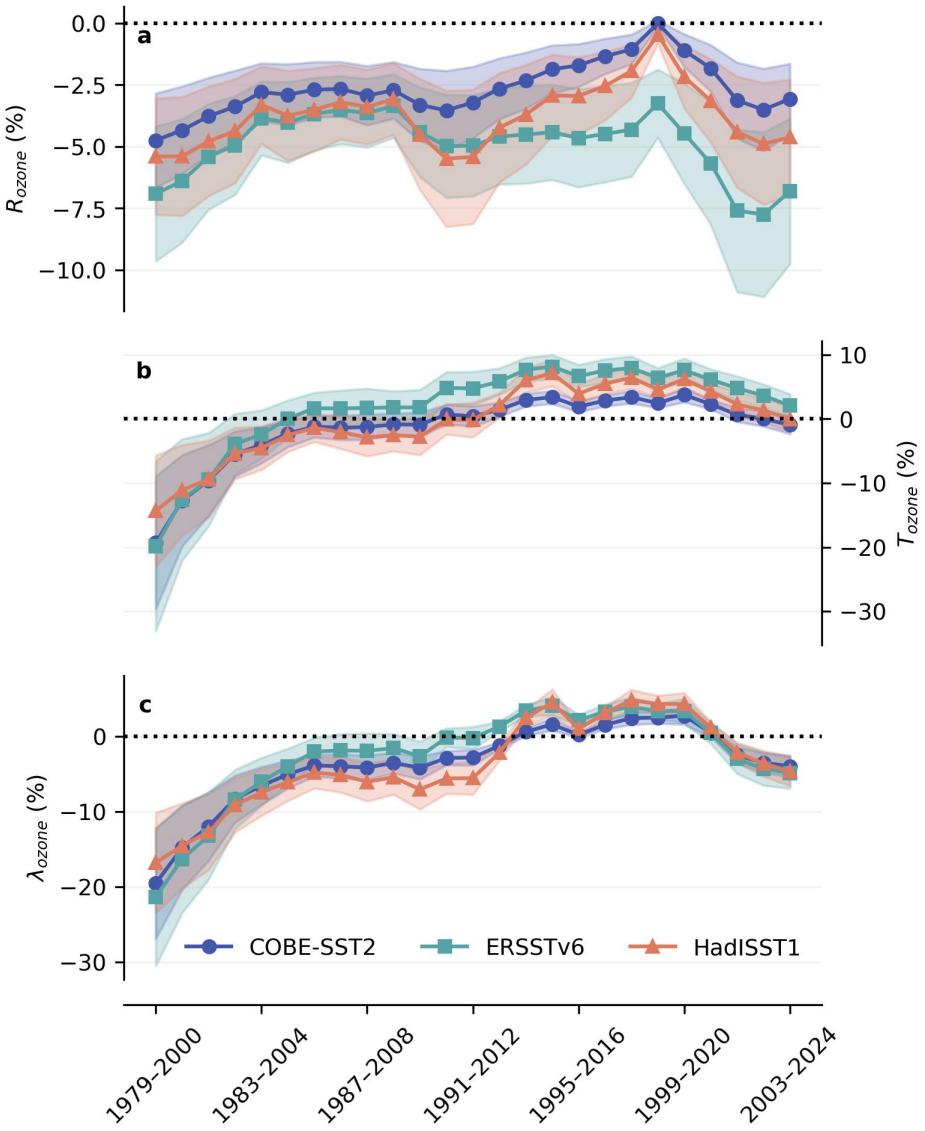

Figure 3. Climate sensitivity due to ozone-induced sea surface temperature pattern changes. Panel a shows percent difference in top-of-atmosphere net radiation *R*, panel b in global-mean surface temperature *T*, and panel c in global radiative feedback parameter *λ*, each estimated using the Green's function between observed SST and its counterpart with the ozone-explained SST removed. Results are calculated over sliding 22-year trend windows from 1979 to 2024. Each color represents a different SST observation product, and shading denotes the ±1σ uncertainty derived from the MLR regression coefficients. The percent differences here quantify the contribution of ozone-induced SST pattern changes in *R*, *T*, and *λ*.

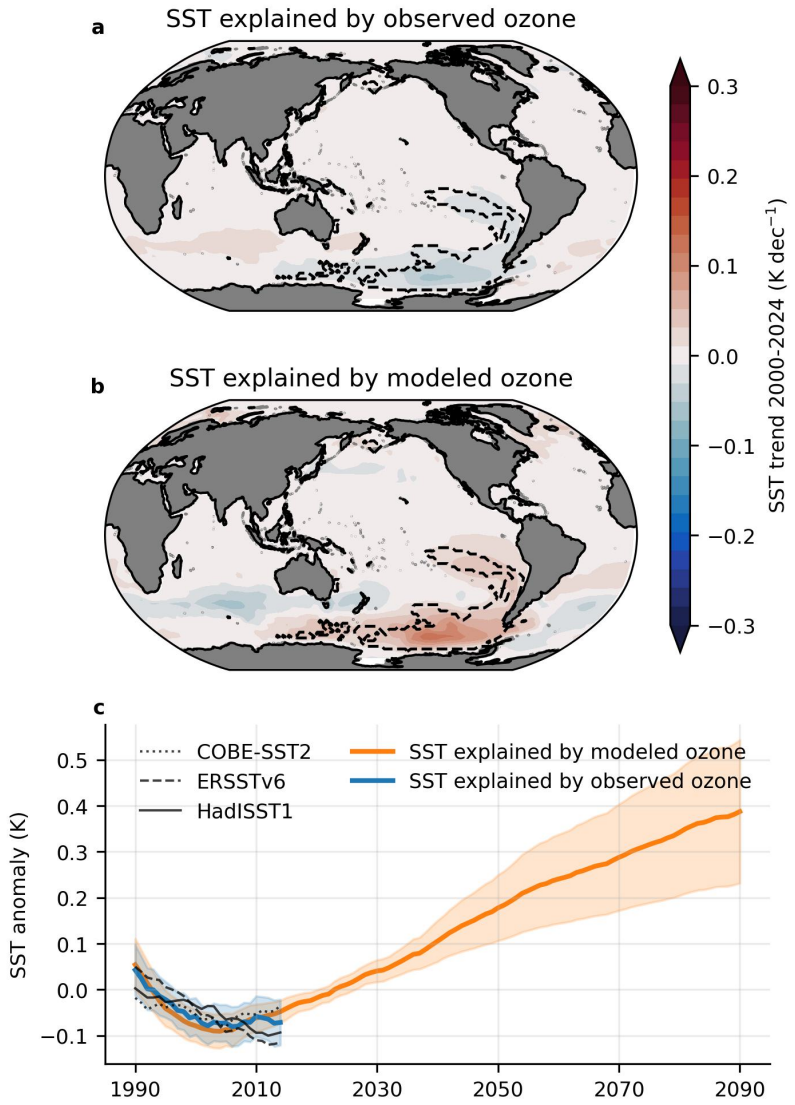

Figure 4. Comparison of ozone-explained sea surface temperature using observed and model-simulated ozone. Panels a and b show SST trend maps from 2000 to 2024 derived from the MLR using observed ozone from SBUV and simulated ozone from CMIP6, respectively. Panel c shows 22-year running-mean SST anomalies averaged over the eastern tropical Pacific and Southern Ocean (region enclosed by the dashed contours in a-b). Blue and orange curves denote SST driven by SBUV and CMIP6 ozone, respectively, with shading indicating ±1σ from the MLR regression coefficients. Black solid, dashed, and dotted curves show the three SST observation products for comparison. The blue and black curves in c are identical to those shown in Figure 1f.

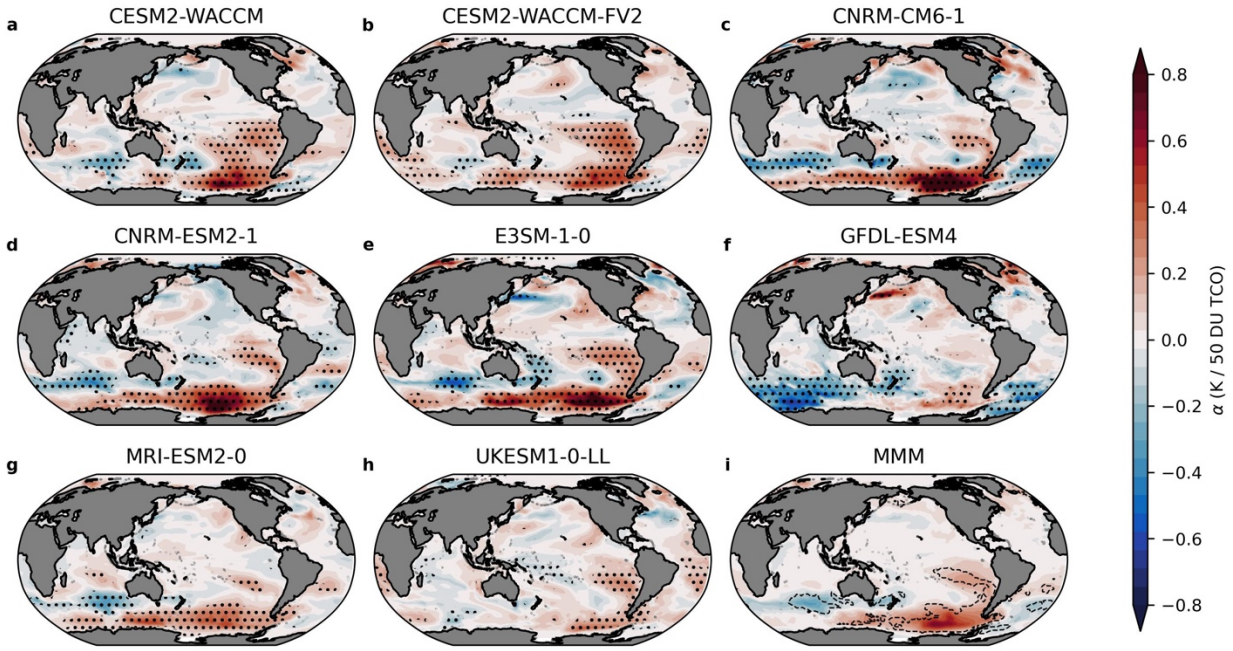

608

609 **Extended Data Figure 1. Regression coefficients on Antarctic ozone in the MLR.**
610 Panels a-h show partial regression coefficients on Antarctic ozone for individual CMIP6
611 GCMs derived from their PiControl simulations. Dots indicate regions where the $p < 0.05$
612 in the MLR, denoting higher confidence in the SST response to Antarctic ozone. Panel i
613 shows the multi-model-mean of the regression coefficients, with dashed contours
614 highlighting regions where all eight GCMs agree on the sign of the SST response to
615 Antarctic ozone.

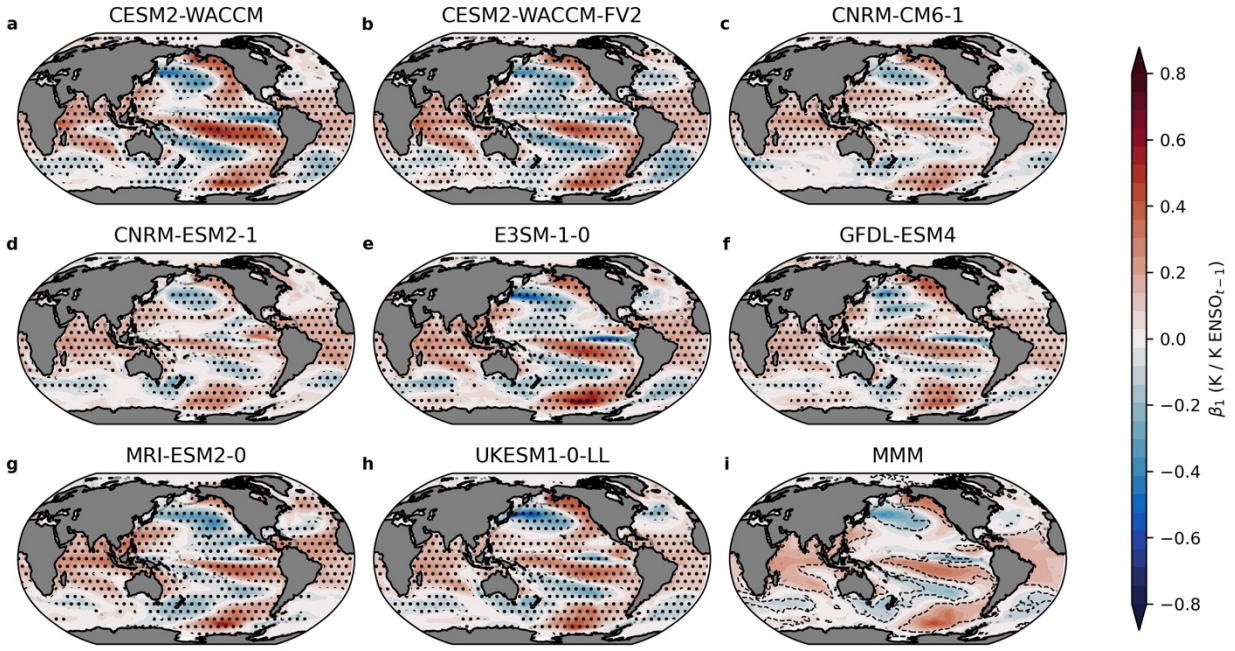

616

617 **Extended Data Figure 2. Regression coefficients on ENSO (lag 1-year) in the MLR.**

618 Same as Extended Data Figure 1, but for ENSO with a 1-year lag.

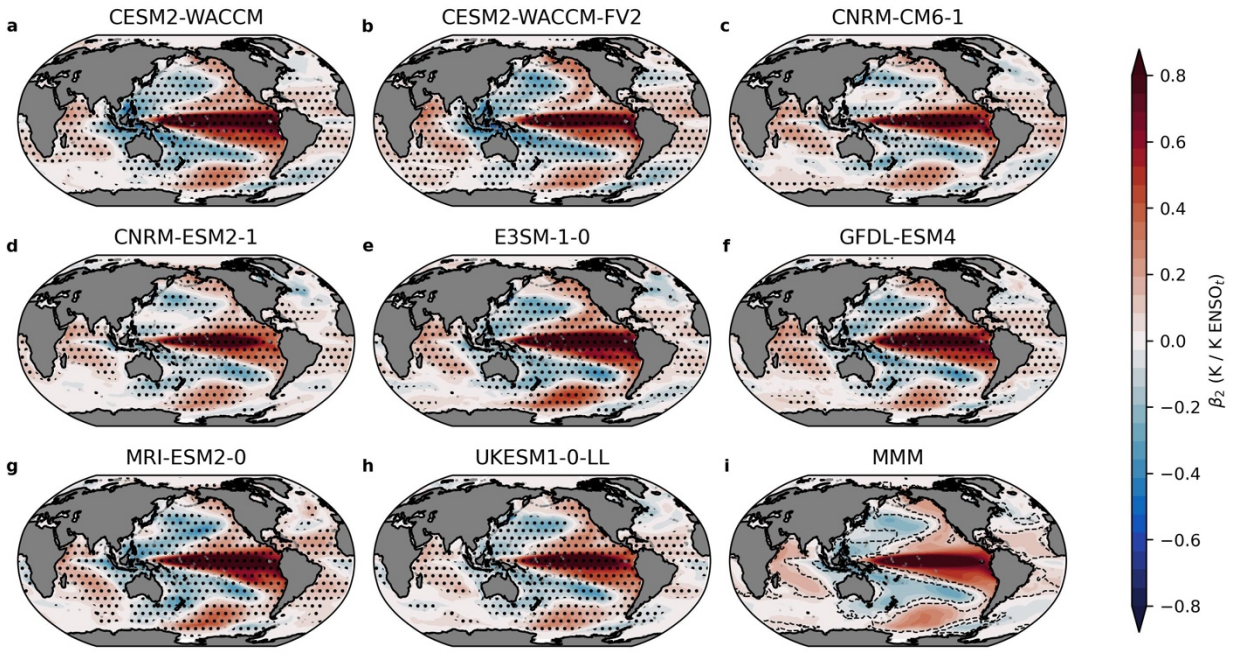

Extended Data Figure 3. Regression coefficients on ENSO (lag 0-year) in the MLR. Same as Extended Data Figure 1, but for ENSO with a 0-year lag.

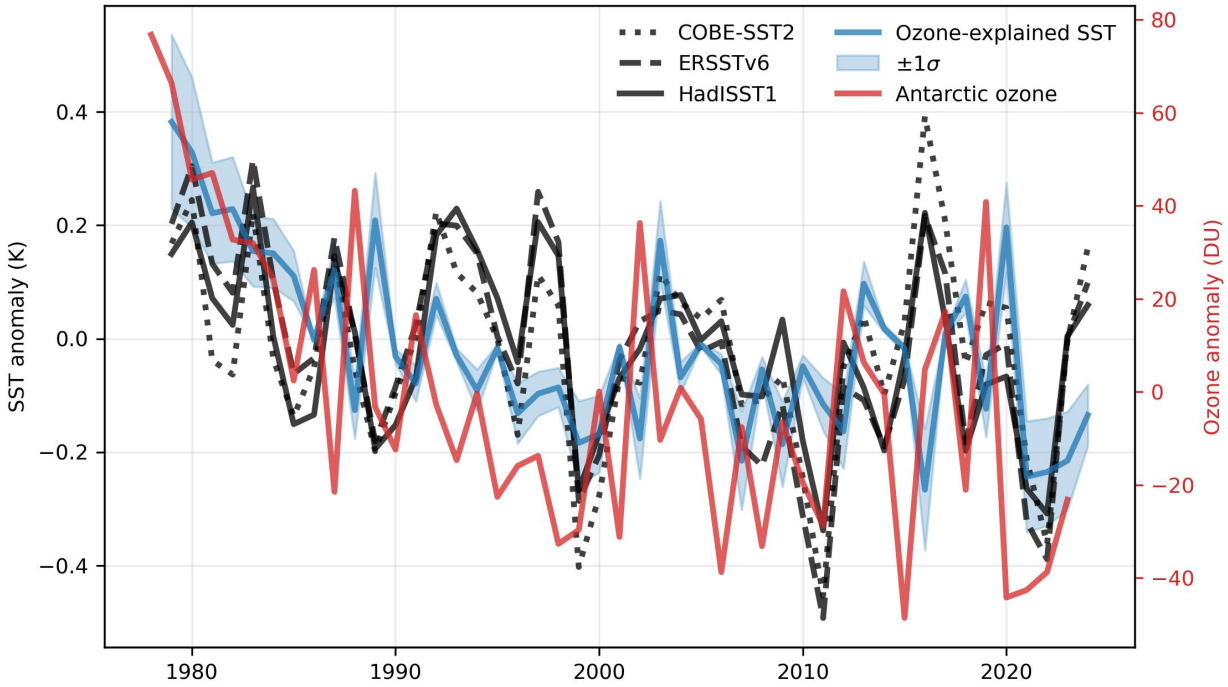

Extended Data Figure 4. Interannual timeseries of sea surface temperature anomalies. Same as Figure 1f, but on interannual timescales.

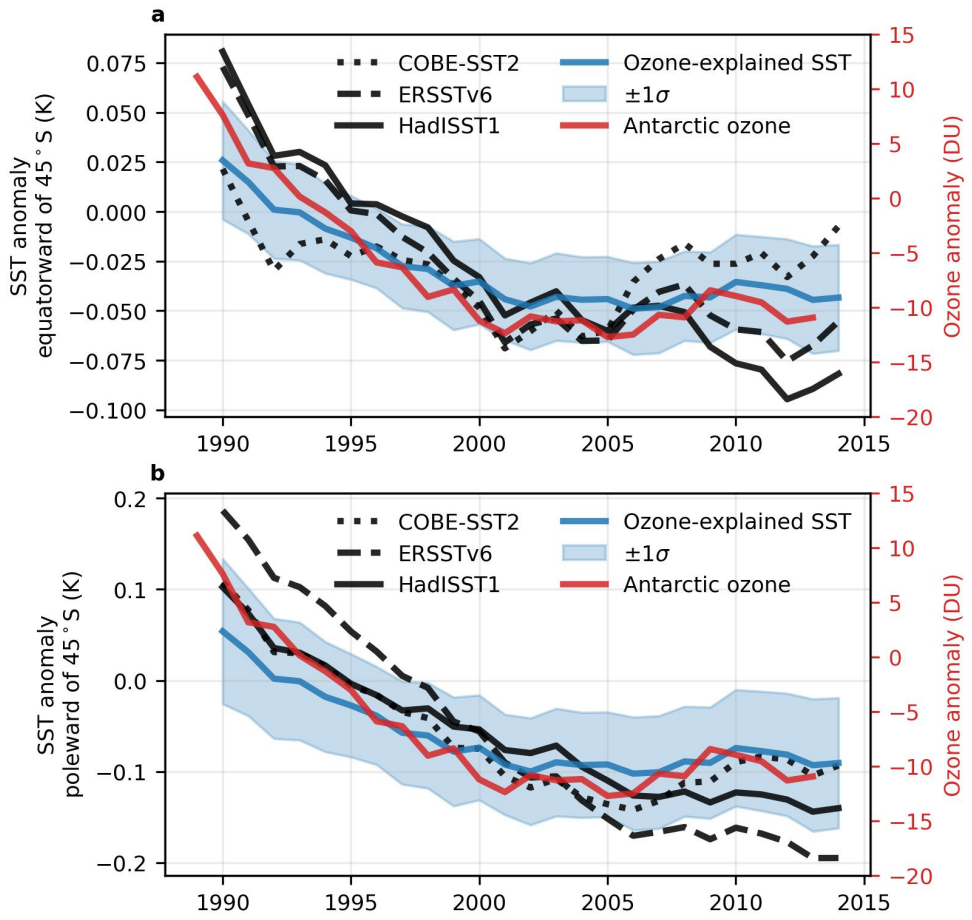

Extended Data Figure 5. Sea surface temperature anomalies in separate regions. Same as Figure 1f, but showing 22-year running-mean SST anomalies averaged separately over the eastern tropical Pacific (equatorward of 45°S; panel a) and the Southern Ocean (poleward of 45°S; panel b).

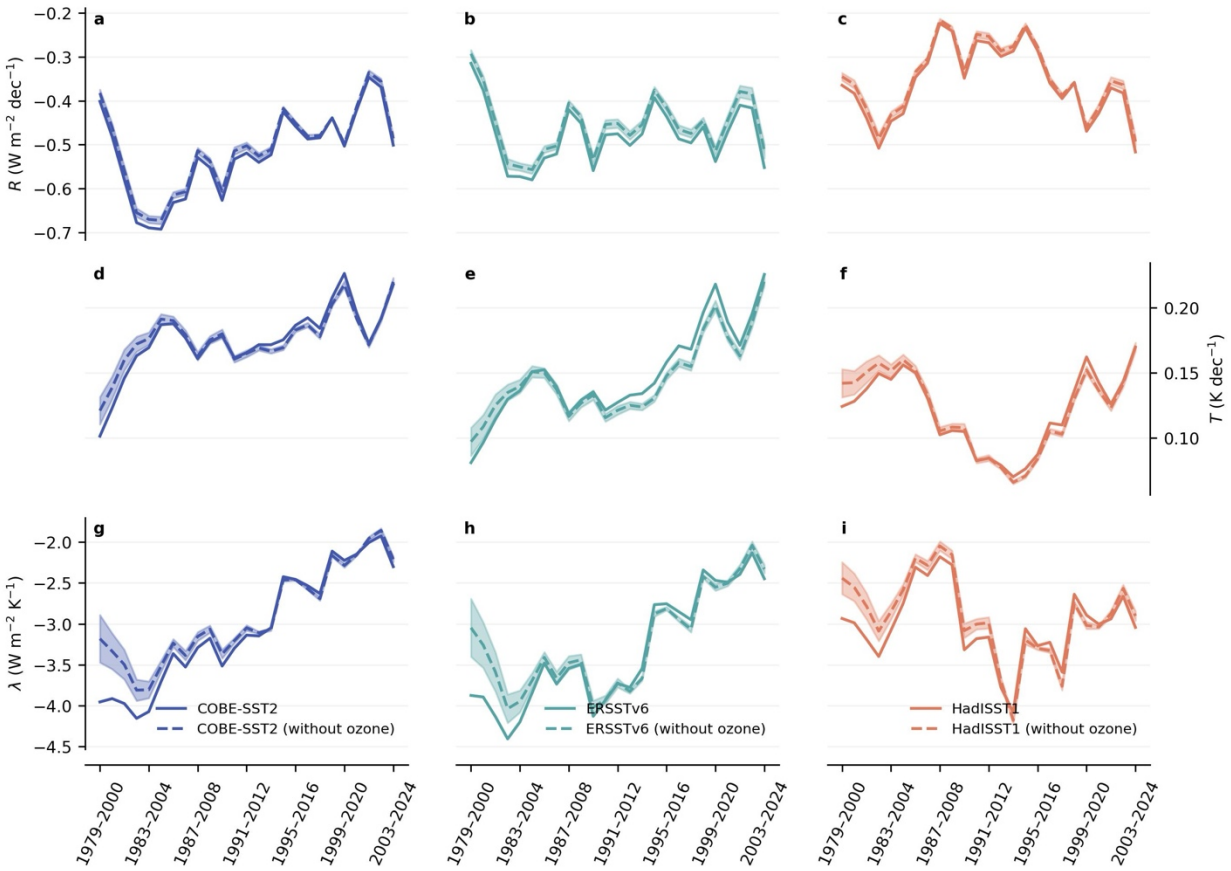

Extended Data Figure 6. Climate sensitivity associated with different sea surface temperature trend patterns. For sliding 22-year windows, trends in top-of-atmosphere net radiation *R* and global-mean surface temperature *T* derived from the Green's function method are shown for each SST observation product (three different columns distinguished by color). Solid curves represent values derived from direct SST observations, which include all forcings and internal variability, while dashed curves represent those derived from SST observations with the ozone-explained component removed, corresponding to a hypothetical world without ozone-induced SST pattern changes. The global radiative feedback parameter λ is calculated as the ratio between trends in *R* and *T* associated with different SST trend patterns. Shading around dashed curves indicates the ±1σ uncertainty from regression coefficients across the eight GCMs.

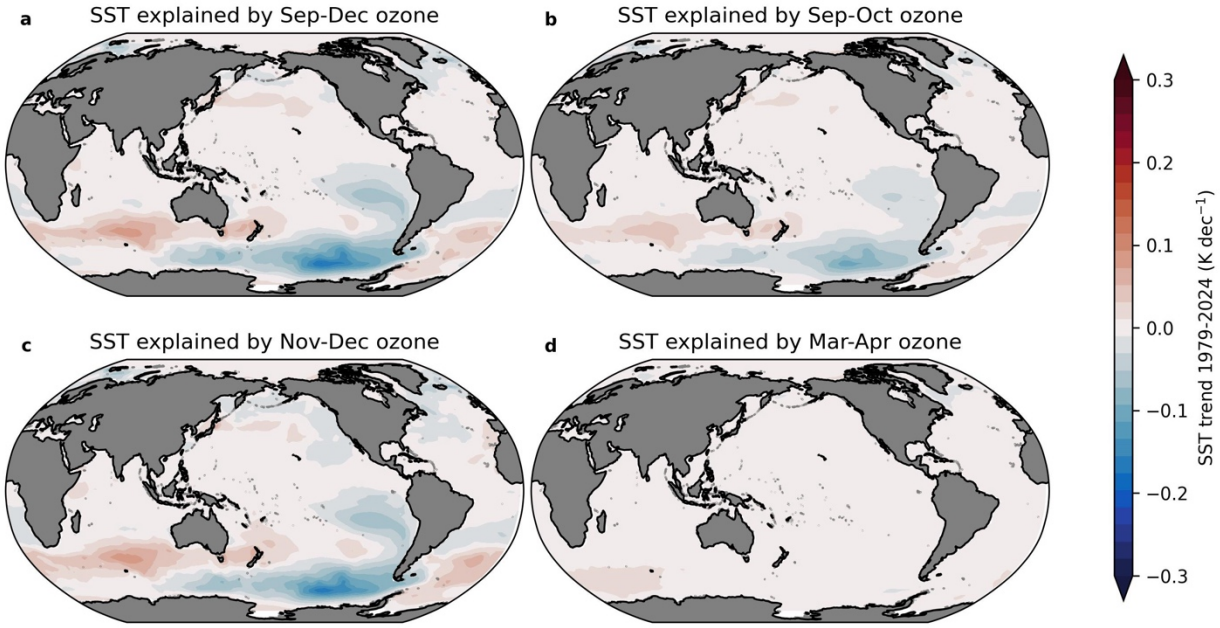

642

643 **Extended Data Figure 7. Sea surface temperature trends from MLR sensitivity tests.**
644 SST trends during 1979-2024 derived from MLR using Antarctic ozone (60°S-90°S)
645 averaged in (a) September-December (main analysis), (b) September-October, (c)
646 November-December, and (d) March-April.

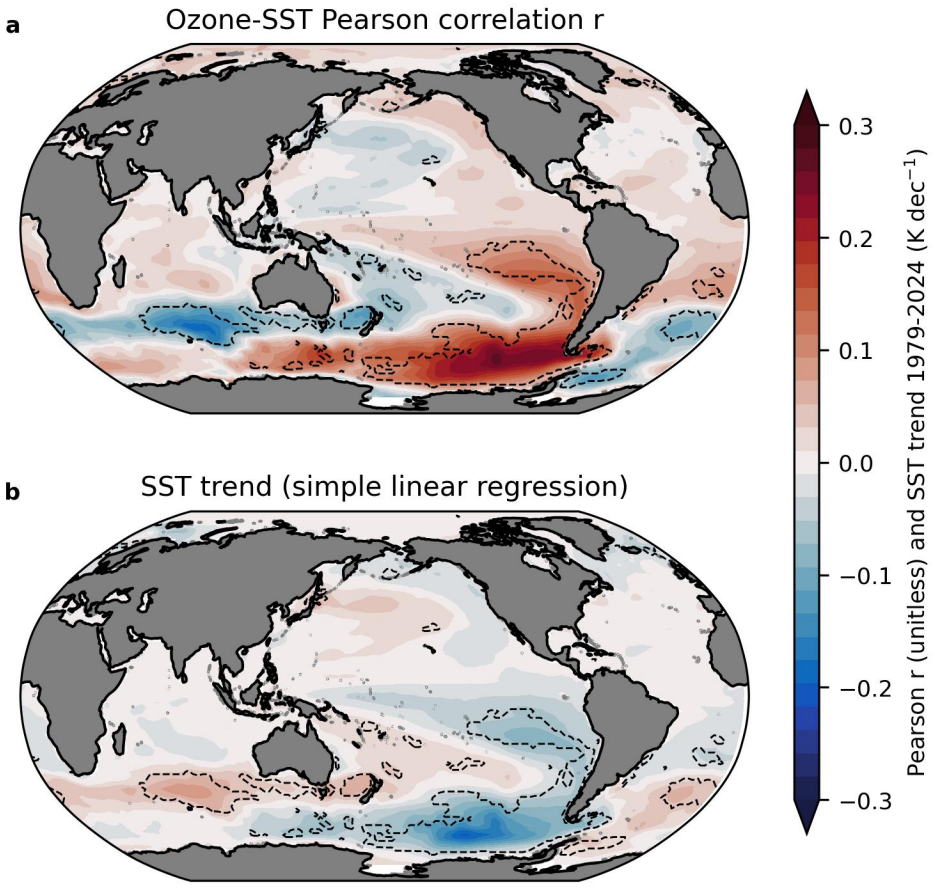

Extended Data Figure 8. Ozone-explained SST from simple linear regression. A simple linear regression using Antarctic ozone as the sole predictor (without ENSO indices) of SST is performed. Panel a shows the multi-model-mean Pearson correlation coefficient r between Antarctic ozone and SST from the PiControl simulations of eight GCMs. Panel b shows the 1979-2024 ozone-explained SST trend map derived from the simple linear regression. Dashed contours highlight regions where all eight GCMs agree on the sign of the SST response to Antarctic ozone. Panels a and b share the same color scale, though units are different.

Extended Data Table 1. List of CMIP6 GCMs used in this study.

Model	Years of PiControl used to construct MLR	Historical and SSP availability	Stratospheric ozone
CESM2-WACCM	499	Historical+SSP2-4.5	Fully interactive
CESM2-WACCM-FV2		Historical	Fully interactive
CNRM-CM6-1		Historical+SSP2-4.5	Linearized scheme
CNRM-ESM2-1		Historical+SSP2-4.5	Fully interactive
E3SM-1-0		Historical	Linearized scheme
GFDL-ESM4		Historical+SSP2-4.5	Fully interactive
MRI-ESM2-0		Historical+SSP2-4.5	Fully interactive
UKESM1-0-LL		Historical+SSP2-4.5	Fully interactive